Two-center interference effect in ionization of diatomic molecules subject to close-to-circularly-polarized femtosecond laser fields

MingZheng Wei,[1,2] Wei Quan,[2,*] RenPing Sun,[2,3] SongPo Xu,[2,3] ZhiLei Xiao,[2,3] Yu Zhou,[2,3] Meng Zhao,[2,4] XiaoLei Hao,[5,†] ChuanXi Duan,[1] and XiaoJun Liu[2]

[1]*College of Physical Science and Technology, Central China Normal University, Wuhan 430079, China*

[2]*State Key Laboratory of Magnetic Resonance and Atomic and Molecular Physics and Center for Cold Atom Physics, Wuhan Institute of Physics and Mathematics, Chinese Academy of Sciences, Wuhan 430071, China*

[3]*School of Physics, University of Chinese Academy of Sciences, Beijing 100080, China*

[4]*Hubei Province Key Laboratory of Systems Science in Metallurgical Process, Wuhan University of Science and Technology, Wuhan 430081, China*

[5]*Institute of Theoretical Physics and Department of Physics, State Key Laboratory of Quantum Optics and Quantum Optics Devices, Collaborative Innovation Center of Extreme Optics, Shanxi University, Taiyuan 030006, China*

Experimentally and theoretically, we explore the photoelectron momentum distributions of N_2 and O_2 and their companion atoms Ar and Xe, which possess nearly equal electron binding energies to the corresponding molecules, subject to close-to-circularly polarized laser fields. Compared to Xe, significant deviations of the results for O_2 have been observed experimentally. In the meantime, the measured photoelectron momentum distributions of N_2 match those of Ar. With the theoretical analysis based on strong field approximation, the results that N_2 behaves just like its companion atom Ar and O_2 behaves significantly different from Xe have been attributed to the two-center interference effect of diatomic molecules, which is disparate for N_2 and O_2 due to the parity difference of their molecular ground-state wave functions.

I. INTRODUCTION

For atoms and molecules subject to strong femtosecond laser fields, a fundamental process to occur is ionization, which may further induce a diverse range of highly nonlinear phenomena [1,2], such as high-order above-threshold ionization (HATI) [3], high-order harmonic generation [4,5], and nonsequential double ionization [6–8], etc. Generally, in the limit of long wavelength and high intensity, which is typical for most current experiments, a quasistatic approximation (QSA) is usually employed to comprehend the ionization dynamics. The essential of QSA is that the laser electric field can be regarded as quasistatic because substantial ionization occurs in a small fraction of one optical cycle. With QSA, the ionization rate of arbitrary atoms can be described by the Ammosov, Delone, and Krainov (ADK) theory [9] and a dominant role is given to the ionization potential (I_p) of the quantum system in question.

Although earlier experimental works show that the molecules are tunnel ionized as if they were atoms with similar ionization potentials [10,11], later experimental works reveal the ionization suppression of a diatomic molecule [12–18], which means that the ionization rate of a diatomic molecule is found to be lower than that of an atom with a comparable I_p (called a companion atom), with otherwise identical conditions. Specifically, experimental investigations

indicate that, in comparison with its companion atom Xe, the ionization rate is suppressed significantly for O_2, while the ionization rates of N_2 and F_2 are very close to that of their companion atom of Ar. Several theoretical attempts have been made to explain these observations. First, with the analysis based on an S-matrix theory [19], it is revealed that the suppression of ionization rate is introduced by the antibonding symmetry of the highest occupied molecular orbit (HOMO) of O_2 through a destructive interference of the two subwaves of the ionizing electron emerging from the two atomic centers and the ionization suppression is absent for N_2 due to the bonding symmetry of its HOMO. Second, the electron screening effect, which gives rise to a changing mean field while the ionizing electron moves away from the core and will induce a higher I_p for O_2, is suggested to introduce a charge-screening correction to the ADK theory [20]. Third, as an extension of the atomic ADK theory, a tunneling molecular ADK model has been developed [21], in which the difference between atomic and molecular ionization is attributed to different asymptotic behaviors of their ground-state wave functions. Finally, it is argued that molecular ionization suppression may also be affected by nuclear vibrational effects [22,23].

Further experimental investigations have been performed to justify the theoretical models mentioned above and great attention has been paid to the one based on the S matrix [19]. For example, experimental observations [14] indicate that the low-energy above-threshold ionization (ATI) peaks for O_2 are suppressed compared to those of Xe and the difference between the spectrum of O_2 and Xe tends to decrease with increasing electron kinetic energy, which confirms

---

*charlywing@wipm.ac.cn

†xlhao@sxu.edu.cn

the corresponding predictions of intense-field S-matrix theory [19]. Further studies [17,18] found that the S-matrix theory calculation can reproduce the observed peculiar wavelength, intensity, and polarization dependence of the suppressed ionization of O_2 with respect to its companion atom of Xe and identifies the role of two-center interference in the ionization suppression of O_2. In contrast, it has been recently observed [24] that the photoelectron yields of O_2 are suppressed in the entire energy spectral range as compared with Xe with fully differential and coincident measurements, which is different from the prediction by the same model. These studies imply that the physics behind the molecular ionization suppression has not been fully comprehended so far.

To deepen our understanding on the physical origin of molecular ionization suppression, it would be helpful to further explore the two-dimensional photoelectron momentum distributions in the polarization plane of a close-to-circularly-polarized laser pulse. Usually, for such a laser field, the photoelectron momentum distributions along any two different orthogonal directions are assumed to be exactly identical (see, e.g., Refs. [24,25]). However, from experimental point of view, it is usually difficult to achieve a perfect circularly polarized laser field and the deviation of ellipticity from 1 can induce the variation of the kinetic energy of photoelectron emitted at different angles in the polarization plane. The result will become even more complicated if the rotation of the photoelectron momentum distribution induced by the Coulomb field and tunneling delay [26,27] are further considered. Therefore, the comparison investigation of diatomic molecule and its companion atom could be less convincing if the photoelectron momentum distributions in only one direction in the polarization plane are explored and compared. Moreover, it is important to apply exactly identical experimental conditions to the diatomic molecule and its companion atom for a reliable comparison study. However, the uncertainties of some experimental conditions, such as the fluctuations of laser intensity and beam pointing, etc., can hardly be eliminated technically in separated experiments. Therefore, it is favorable to apply a gas mixture of the diatomic molecule and its companion atom, which may diminish the fluctuations of the experimental conditions for the diatomic molecule and its companion atom to the largest extent [15,28].

In this paper, we experimentally investigate the two-dimensional photoelectron momentum distributions in the polarization plane for N_2 and O_2 and Ar and Xe subject to close-to-circularly-polarized laser fields. Especially, to maintain the parameters of the laser pulse applied to atoms and molecules accurately identical, the gas mixture containing N_2 and Ar and that of O_2 and Xe are employed in the measurements. It is found that the normalized photoelectron momentum distributions of O_2 is clearly narrower than those of Xe, while those of N_2 and Ar match each other. The measured photoelectron momentum distributions can be well reproduced with the strong field approximation (SFA) calculations. Further analysis reveals that the interference between electrons emitted from the vicinity of two distinct ionic cores leads to narrower photoelectron momentum distributions of O_2 with antisymmetric electronic ground states than those of Xe. On the other hand, the absence of the difference between the photoelectron momentum distributions of N_2 and Ar can

be attributed to the distinctive symmetry of the N_2 molecular ground-state wave function.

II. EXPERIMENTAL SETUP

In our experiments, a commercial Ti:sapphire femtosecond laser system (FEMTOPOWER compact PRO CE-Phase HP/HR) is employed to generate laser pulses with a pulse output energy up to 0.8 mJ, a repetition rate of 5 kHz, and a pulse duration of around 30 fs at 800 nm. The laser beam has near-Gaussian distributions in both temporal and spatial domains. The laser pulse energy is precisely controlled by means of a combination of a $\lambda/2$ plate and a broadband thin film polarizer. The elliptical polarization is achieved by passing the beam through a broadband achromatic quarter-wave plate and the ellipticity is 0.98, which is determined by a comparison of the measured and semiclassical calculated photoelectron momentum distributions of noble gas atoms [29]. The laser beam (along x axis), with a diameter of around 8 mm, is tightly focused on the collimated atomic/molecular supersonic beam (along y axis) by an on-axis parabolic mirror with a focal length of 75 mm in the ultrahigh vacuum chamber of a cold-target recoil-ion momentum spectroscopy (COLTRIMS) [29–31]. The Rayleigh length is estimated to be about 20 μm. A constant and uniform electric field (along z axis) is applied to guide and accelerate photoions and photoelectrons to the ion and electron position-sensitive microchannel plates (MCP) detectors with delay line anodes equipped, respectively. To achieve the 4π solid angle photoelectron measurements, a constant and uniform magnetic field of 7.8 Gauss generated by a pair of Helmholtz coils is further applied to confine the photoelectron cyclotron radius. From the measured time of flights and the positions of the particles, the three-dimensional momenta can be retrieved. During the experiments, the momenta of photoelectron and photoion are measured in coincidence and great attention is paid to keep the count rate less than 0.2 (for photoelectron) and 0.04 (for photoion) per laser shot to avoid false coincidence, which is estimated to be around 6%. A gas mixture containing N_2 and Ar (1:1) and that of O_2 and Xe (3:1) are applied to reduce any possible difference of the experimental conditions in the measurements for the diatomic molecules and their companion atoms. Note that there is no attempt to align the molecules during the experiments.

III. SFA THEORY

In the length gauge [32–34], the transition amplitude from the initial state ψ_0 of a molecule to the final Volkov state $\psi_p^{(L)}$ with momentum p can be given by

$$M_p^{(0)} = -i \int_{-\infty}^{\infty} dt \langle \psi_p^{(L)}(t) | \mathbf{r} \cdot \mathbf{E}(t) | \psi_0(t) \rangle$$

$$= -i \int_{-\infty}^{\infty} dt \exp[i S_{\mathbf{p}}(t)] V_{\tilde{\mathbf{p}}0}(t), \qquad (1)$$

where the action is given by

$$S_{\mathbf{p}}(t) = -\frac{1}{2} \int_t^{\infty} d\tau [\mathbf{p} + \mathbf{A}(\tau)]^2 + I_p t \qquad (2)$$

with the ionization potential of I_p, and the prefactor can be calculated by

$$V_{\widetilde{\mathbf{p}}0}(t) = \int d^3\mathbf{r} \exp[-i\widetilde{\mathbf{p}} \cdot \mathbf{r}]\mathbf{r} \cdot \mathbf{E}(t)\psi_0(\mathbf{r}), \qquad (3)$$

where, in length gauge, $\widetilde{\mathbf{p}}$ is defined by $\widetilde{\mathbf{p}} = \mathbf{p} + \mathbf{A}(t)$. The electric field $\mathbf{E(t)}$ can be obtained by taking derivative of the two-dimensional vector potential $(0, A_0\epsilon \sin \omega t, A_0 \cos \omega t)$ with A_0 the amplitude of the vector potential, ϵ the ellipticity and ω the frequency of the laser field. Within the fixed-nuclei approximation, the diatomic molecular initial state ψ_0 can be taken as a linear combination of atomic orbits (LCAO),

$$\sum_a c_a \left[\psi_a^0(\mathbf{r} + \mathbf{R}_0/2) + \gamma \psi_a^0(\mathbf{r} - \mathbf{R}_0/2) \right], \qquad (4)$$

where $\mathbf{R}_0$ denotes the relative nuclear coordinate and γ can be 1 or -1 depending on the symmetry. In our calculation, Eq. (1) is integrated using the saddle-point method.

To describe the molecular HOMO conveniently, we establish a three-dimensional orthogonal coordinate system (X, Y, Z) in molecular frame, where the molecular axis is along the Z direction and the origin locates at the midpoint between the two atomic centers of the diatomic molecule. During the calculation, the HOMO of N_2 ($3\sigma_g$) can be expressed as a linear combination of s and p_Z orbits with almost equal amplitudes, while that of O_2 ($1\pi_g$) can be well described by a linear combination of p_X or p_Y orbits [35]. In order to calculate the prefactor $V_{\widetilde{\mathbf{p}}0}$, the momentum $\widetilde{\mathbf{p}}$ has to be transformed from the laboratory frame (x, y, z) to the molecular frame (X, Y, Z), which can be achieved with the equations listed below,

$$\begin{aligned}
\widetilde{p}_X &= \widetilde{p}_x \\
\widetilde{p}_Y &= \widetilde{p}_y \cos\theta - \widetilde{p}_z \sin\theta \\
\widetilde{p}_Z &= \widetilde{p}_y \sin\theta + \widetilde{p}_z \cos\theta,
\end{aligned} \qquad (5)$$

where $\widetilde{p}_x = p_x$, $\widetilde{p}_y = p_y + A_0\epsilon \sin \omega t$ and $\widetilde{p}_z = p_z + A_0 \cos \omega t$. For simplicity, the molecule is assumed to be aligned in the laser polarization plane and θ is the angle between the molecular axis and the z axis in laboratory frame.

IV. RESULTS AND DISCUSSIONS

We have measured the two-dimensional photoelectron momentum distributions of diatomic molecules $N_2(I_p = 15.58$ eV) and $O_2(I_p = 12.03$ eV) and their companion atoms $Ar(I_p = 15.76$ eV) and $Xe(I_p = 12.13$ eV) subject to close-to-circularly-polarized laser fields with an ellipticity of 0.98 at 800 nm. The laser intensity is 6.7×10^{13} W/cm² for O_2 (Xe) and 1.5×10^{14} W/cm² for N_2 (Ar). As well discussed [26,27], for atoms and molecules subject to close-to-circularly-polarized laser field, the tunneling delay and the Coulomb potential will result in an angular offset of the entire photoelectron momentum distribution. To compare the measured photoelectron momentum distributions with SFA calculations more conveniently, the influence of this angular offset has been deliberately removed by rotating the two-dimensional photoelectron momentum distributions until the spacing between the crests of the two humps of the distributions along y axis reaches maximum for each sample [29]. After the rotation manipulation, the two-dimensional photoelectron momentum
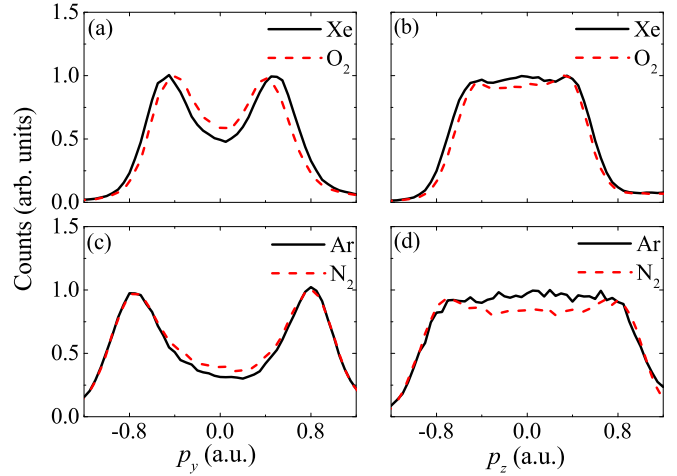
FIG. 1. The measured photoelectron momentum distributions of O_2 and Xe (a), (b) and N_2 and Ar (c), (d) along y (a), (c) and z (d), (b) directions. The ellipticity of the laser field is 0.98. The laser intensities are 6.7×10^{13} W/cm² for O_2/Xe and 1.5×10^{14} W/cm² for N_2/Ar. Please find more details in the text.

distributions are projected into the y axis and z axis to achieve the photoelectron momentum distribution along each direction. The results are pictured in Fig. 1.

As shown in Fig. 1, the photoelectron momentum distributions of all the targets along y direction show a prominent double-hump structure (DHS). In contrast, along z direction, the dip in the center of the DHS shrinks or even disappears and the distributions become more like a flat-top structure. The difference of the distributions along y and z directions can be attributed to the deviation of the ellipticity from 1, which can lead to a larger electric field amplitude along the direction of major axis (z axis) in the polarization plane. Due to the exponential field strength dependence of the ionization yields, two significant humps in photoelectron momentum distributions along the y direction appear.

A closer inspection reveals that the photoelectron momentum distributions of O_2 are narrower than those of Xe along both directions, while the photoelectron momentum distributions of N_2 are almost identical to those of Ar. Because the photoelectron momentum distributions are measured from a mixture gas of O_2 and Xe, the deviation of the intensity for O_2 from that for Xe due to the small changes in focus geometry, caused by nominal beam alignment deviation or beam pointing fluctuation etc., can be safely ruled out. Considering the fact that the difference between the ionization potentials for O_2 and Xe is too small to explain the difference in the photoelectron momentum distributions, it is necessary to explore its physical origin with a sophisticated theoretical method.

Numerical calculations with SFA, which have been successfully applied to the study of ionization dynamics for diatomic molecules subject to intense laser fields [36,37], have been performed for N_2 and O_2 and their companion atoms Ar and Xe with laser parameters chosen according to the experiments. To compare with the experimental results directly, the calculated photoelectron momentum distributions of N_2 and O_2 are averaged among all possible directions of molecular
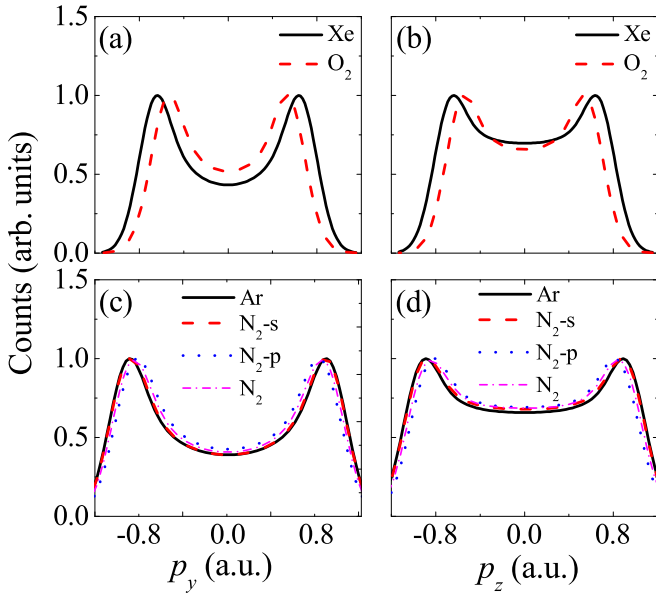
FIG. 2. The calculated photoelectron momentum distributions of O_2 and Xe (a), (b) and N_2 and Ar (c), (d) along y (a), (c) and z (d), (b) directions with the method of SFA. In (c), (d), the separate contributions from s and p_Z component of N_2 are also depicted. The parameters are chosen according to those of Fig. 1. Please find more details in the text.

FIG. 3. The two-dimensional photoelectron momentum distributions of O_2 (a) and p_Z component of N_2 (b) with the molecular axis aligned along the y direction. (c) and (d) are the same to (a) and (b) except that the effect of the trigonometric part is not included. The laser parameters are chosen according to Fig. 1. The ionization rate of each panel is normalized for a better comparison.

alignment. As shown in Fig. 2, most of the dominant features of the measured photoelectron momentum distributions are reproduced. The DHS is prominent along the y direction, while the dip between the two humps is shallower for the photoelectron momentum distributions along z direction for all the gas targets. Closer inspection indicates that the photoelectron momentum distributions are significantly larger for Xe than those for O_2 along both y and z directions. In addition to the calculation results for N_2 and Ar, in Figs. 2(c) and 2(d), we further present the separate photoelectron momentum distributions of s and p_Z components of N_2, respectively. As one can see, the photoelectron momentum distributions of s orbit component of N_2 are almost identical to those of Ar. On the other hand, though the photoelectron momentum distributions of p_Z component is a bit narrower than those of Ar, the discrepancy is much smaller than that between O_2 and Xe. Therefore, with the combining contributions of the s and p_Z components of N_2, as shown in Figs. 2(c) and 2(d), the discrepancy between N_2 and Ar is significantly smaller than that of O_2 and Xe, which is in accordance with the measurements (see Fig. 1).

The different behaviors for O_2 and N_2 is rooted in the difference of their valence electron initial-state wave functions. From Eq. (4), it is clear that the wave function of the initial state is determined by the atomic orbit ψ_a^0 and the symmetry parameter γ. Depending on the value of γ, an additional trigonometric part associated with the interference between the waves of the ionizing electron emerging from the two nuclei will be introduced in the transition matrix elements $M_p^{(0)}$ for homonuclear diatomic molecules [32,33],

$$M_p^{(0)} \propto \begin{cases} \cos((\mathbf{p}+\mathbf{A}) \cdot \mathbf{R}_0/2) & \gamma = 1 \\ \sin((\mathbf{p}+\mathbf{A}) \cdot \mathbf{R}_0/2) & \gamma = -1 \end{cases}, \quad (6)$$

where $\mathbf{p}$ is the final momentum of the photoelectron and $\mathbf{A}$ the laser vector potential at the instant of tunneling. The HOMO of O_2 can be described with a linear combination of p_X or p_Y states with $\gamma = -1$. In contrast, the HOMO of N_2 includes the contributions from both the s component with $\gamma = 1$ and the p_Z component with $\gamma = -1$. The corresponding trigonometric part is $\sin((\mathbf{p}+\mathbf{A}) \cdot \mathbf{R}_0/2)$ for O_2 and p_Z component of N_2, and $\cos((\mathbf{p}+\mathbf{A}) \cdot \mathbf{R}_0/2)$ for s component of N_2.

To show the significant effect of the trigonometric part of $\sin((\mathbf{p}+\mathbf{A}) \cdot \mathbf{R}_0/2)$, in Fig. 3, we present the calculated two-dimensional photoelectron momentum distributions of O_2 [Fig. 3(a)] and p_Z component of N_2 [Fig. 3(b)]. In the meantime, the corresponding photoelectron momentum distributions without the trigonometric part for O_2 and p_Z component of N_2 are also shown in Figs. 3(c) and 3(d), respectively. In contrast to the results in Fig. 1 and Fig. 2, the photoelectron momentum distributions in Fig. 3 (and also Fig. 4 below) are depicted with the coordinate system (X, Y, Z) in the molecular frame. As shown in Fig. 3(c), two maxima appear along p_Z axis in the photoelectron momentum distributions of O_2, which can be attributed to the fact that, here, the dominate contributions are from the p_Y orbit of O_2 HOMO and the corresponding wave function of this orbit is mainly distributed along the p_Y axis. Note that, if the Coulomb potential is ignored, after the acceleration from the laser field, the ionized electron will eventually drift in a direction perpendicular to the instantaneous field from which it was released [38]. Impressively, with the trigonometric part of $\sin((\mathbf{p}+\mathbf{A}) \cdot \mathbf{R}_0/2)$ included, a dramatically change can be identified in the photoelectron momentum distributions, as shown in Fig. 3(a), where the local maxima along the p_Z direction become minima. This can be attributed to the fact that the trigonometric part mainly degrades photoelectron yields along the molecular axis (along p_Z direction)
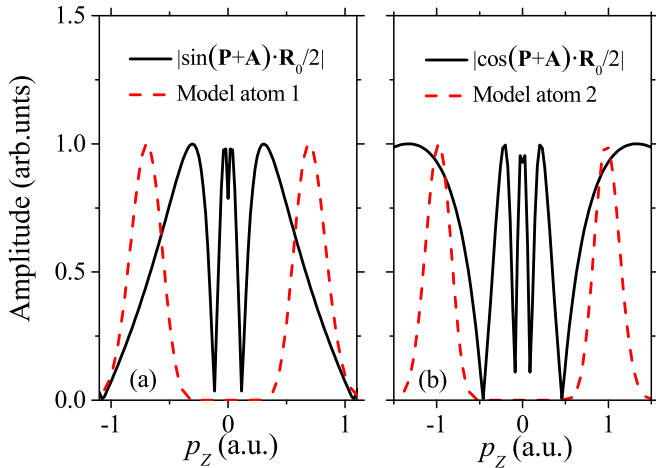
FIG. 4. (a) The photoelectron momentum distribution of the model atom 1 with same wave-function and equal I_p to those of O_2 along y axis with $\mathbf{p}_Y = 0$ and the modulation curves induced by trigonometric part of $\sin((\mathbf{p} + \mathbf{A}) \cdot \mathbf{R}_0/2)$. (b) The photoelectron momentum distribution of the model atom 2 with same wave-function to that of the s component of N_2 and equal I_p to that of N_2 along y axis with $\mathbf{p}_Y = 0$ and the modulation curves induced by trigonometric part of $\cos((\mathbf{p} + \mathbf{A}) \cdot \mathbf{R}_0/2)$. The laser parameters are chosen according to Fig. 1. Please find more details in the text.

and its effect is so significant that the maxima in Fig. 3(c) become perceivably lower than the local minima along p_Y direction when the trigonometric part is not included. In contrast, for p_Z component of N_2, as show in Figs. 3(b) and 3(d), only a moderate change can be identified in the photoelectron momentum distributions if the photoelectron momentum distributions with and without trigonometric part included are compared. This result can be attributed to the fact that the dominant wave-function amplitude of the p_Z orbit locates along the molecular axis, which will induce two maxima in the photoelectron momentum distribution along p_Y direction (perpendicular to the molecular axis) and these two maxima along p_Z direction will not be degraded significantly if the trigonometric part is further considered. Therefore, as discussed above, the influence of p_Z component of N_2 on the photoelectron momentum distributions is expected to be more faint than that of p component of O_2 (see Fig. 2).

To further illustrate the different influence of the trigonometric parts of O_2 and the s component of N_2 on the photoelectron momentum distributions, in Fig. 4(a), we depict the modulations induced by the trigonometric term of $\sin((\mathbf{p} + \mathbf{A}) \cdot \mathbf{R}_0/2)$ and also the photoelectron momentum distribution of the model atom 1, which possesses the same ground-state wave function and equal I_p to those of O_2, along the p_Z axis with $\mathbf{p}_Y = 0$. In the meantime, in Fig. 4(b), the modulation induced by the trigonometric term of $\cos((\mathbf{p} + \mathbf{A}) \cdot \mathbf{R}_0/2)$ and also the photoelectron momentum distribution of the model atom 2, which possesses the same ground-state wave

function to that of s component of N_2 and equal I_p to that of N_2, along the p_Z axis with $\mathbf{p}_Y = 0$ are also pictured. The laser parameters are chosen according to Fig. 1. As one can see, in Fig. 4(a), a prominent DHS can be identified for the photoelectron momentum distributions of the model atom 1 along y direction. On the other hand, the trigonometric term of $\sin((\mathbf{p} + \mathbf{A}) \cdot \mathbf{R}_0/2)$ induces a modulation with rapid oscillation, which will be imposed on the photoelectron momentum distributions of model atom 1 to achieve that of O_2. Note that the rapid oscillation around $\mathbf{p}_Z = 0$ will not influence the photoelectron momentum distribution of O_2 due to the absence of the photoelectron yields in this momentum range for model atom 1. With closer inspection, one can see that the modulation of $\sin((\mathbf{p} + \mathbf{A}) \cdot \mathbf{R}_0/2)$ term is out of phase with the DHS for the photoelectrons with momenta in the interval of $\mathbf{p}_Z > 0.3$ a.u. and $\mathbf{p}_Z < -0.3$ a.u., which will bring a pronounced suppression of the ionization yields and make the photoelectron momentum distributions significantly narrower. In contrast, in Fig. 4(b), the modulation of $\cos((\mathbf{p} + \mathbf{A}) \cdot \mathbf{R}_0/2)$ term is almost in phase with the peaks of DHS in the photoelectron momentum distributions of model atom 2 in the interval of $\mathbf{p}_Z > 0.5$ a.u. and $\mathbf{p}_Z < -0.5$ a.u. and its influence on the photoelectron momentum distributions of s component of N_2 could be faint. Therefore, considering the fact that the suppression effect of p_Z component of N_2 is expected to be more faint than that of p component of O_2, one can well comprehend the results that the photoelectron momentum distributions of O_2 is significantly narrower than those of its companion atom Xe, while the photoelectron momentum distributions are close to each other for N_2 and Ar.

V. CONCLUSION

In conclusion, we have experimentally and theoretically investigated the photoelectron momentum distributions of diatomic molecules N_2 and O_2 and their companion atoms Ar and Xe subject to the close-to-circularly-polarized laser fields with the ellipticity of 0.98 at 800 nm. It is shown that the photoelectron momentum distributions of O_2 are significantly narrower than those of Xe along y and z directions (both of them are in the polarization plane), while the photoelectron momentum distributions match each other for N_2 and Ar. This result can be well reproduced by SFA numerical simulations and explained by the influence of the different parity of their corresponding HOMOs on the strong field molecular ionization dynamics.

[1] P. B. Corkum, Phys. Rev. Lett. **71**, 1994 (1993).

[2] K. J. Schafer, B. Yang, L. F. DiMauro, and K. C. Kulander, Phys. Rev. Lett. **70**, 1599 (1993).

[3] G. G. Paulus, W. Nicklich, H. L. Xu, P. Lambropoulos, and H. Walther, Phys. Rev. Lett. **72**, 2851 (1994).

[4] J. L. Krause, K. J. Schafer, and K. C. Kulander, Phys. Rev. Lett. **68**, 3535 (1992).

[5] J. J. Macklin, J. D. Kmetec, and C. L. Gordon, Phys. Rev. Lett. **70**, 766 (1993).

[6] A. Becker, R. Dörner, and R. Moshammer, J. Phys. B **38**, S753 (2005).

[7] C. Figueira de Morisson Faria and X. Liu, J. Mod. Opt. **58**, 1076 (2011).

[8] W. Becker, X. J. Liu, P. J. Ho, and J. H. Eberly, Rev. Mod. Phys. **84**, 1011 (2012).

[9] M. V. Ammosov, N. B. Delone, and V. P. Krainov, Sov. Phys. JETP **64**, 1191 (1986).

[10] S. L. Chin, Y. Liang, J. E. Decker, F. A. Ilkov, and M. V. Ammosov, J. Phys. B **25**, L249 (1992).

[11] T. D. G. Walsh, F. A. Ilkov, J. E. Decker, and S. L. Chin, J. Phys. B **27**, 3767 (1994).

[12] A. Talebpour, C.-Y. Chien, and S. L. Chin, J. Phys. B **29**, L677 (1996).

[13] C. Guo, M. Li, J. P. Nibarger, and G. N. Gibson, Phys. Rev. A **58**, R4271(R) (1998).

[14] F. Grasbon, G. G. Paulus, S. L. Chin, H. Walther, J. Muth-Böhm, A. Becker, and F. H. M. Faisal, Phys. Rev. A **63**, 041402(R) (2001).

[15] M. J. DeWitt, E. Wells, and R. R. Jones, Phys. Rev. Lett. **87**, 153001 (2001).

[16] E. Wells, M. J. DeWitt, and R. R. Jones, Phys. Rev. A **66**, 013409 (2002).

[17] Z. Y. Lin, X. Y. Jia, C. L. Wang, Z. L. Hu, H. P. Kang, W. Quan, X. Y. Lai, X. J. Liu, J. Chen, B. Zeng, W. Chu, J. P. Yao, Y. Cheng, and Z. Z. Xu, Phys. Rev. Lett. **108**, 223001 (2012).

[18] H. P. Kang, Z. Y. Lin, S. P. Xu, C. L. Wang, W. Quan, X. Y. Lai, X. J. Liu, X. Y. Jia, X. L. Hao, J. Chen, W. Chu, J. P. Yao, B. Zeng, Y. Cheng, and Z. Z. Xu, Phys. Rev. A **90**, 063426 (2014).

[19] J. Muth-Böhm, A. Becker, and F. H. M. Faisal, Phys. Rev. Lett. **85**, 2280 (2000).

[20] C. Guo, Phys. Rev. Lett. **85**, 2276 (2000).

[21] X. M. Tong, Z. X. Zhao, and C. D. Lin, Phys. Rev. A **66**, 033402 (2002).

[22] A. Saenz, J. Phys. B **33**, 4365 (2000).

[23] T. K. Kjeldsen and L. B. Madsen, Phys. Rev. A **71**, 023411 (2005).

[24] Y. Deng, Y. Liu, X. Liu, H. Liu, Y. Yang, C. Wu, and Q. Gong, Phys. Rev. A **84**, 065405 (2011).

[25] A. Staudte, S. Patchkovskii, D. Pavičić, H. Akagi, O. Smirnova, D. Zeidler, M. Meckel, D. M. Villeneuve, R. Dörner, M. Yu. Ivanov, and P. B. Corkum, Phys. Rev. Lett. **102**, 033004 (2009).

[26] P. Eckle, M. Smolarski, P. Schlup, J. Biegert, A. Staudte, M. Schöffler, H. Muller, R. Dörner, and U. Keller, Nature Phys. **4**, 565 (2008).

[27] P. Eckle, A. N. Pfeiffer, C. Cirelli, A. Staudte, R. Döerner, H. G. Muller, M. Büttiker, and U. Keller, Science **322**, 1525 (2008).

[28] K. Lin, X. Jia, Z. Yu, F. He, J. Ma, H. Li, X. Gong, Q. Song, Q. Ji, W. Zhang, H. Li, P. Lu, H. Zeng, J. Chen, and J. Wu, Phys. Rev. Lett. **119**, 203202 (2017).

[29] W. Quan, M. Yuan, S. Yu, S. Xu, Y. Chen, Y. Wang, R. Sun, Z. Xiao, C. Gong, L. Hua, X. Lai, X. Liu, and J. Chen, Opt. Express **24**, 23248 (2016).

[30] T. Jahnke, T. Weber, T. Osipov, A. L. Landers, O. Jagutzki, L. P. H. Schmidt, C. L. Cocke, M. H. Prior, H. Schmidt-Böcking, R. Dörner, J. Electron. Spectrosc. Relat. Phenom. **141**, 229 (2004).

[31] J. Ullrich, R. Moshammer, A. Dorn, R. Dörner, L. P. H. Schmidt, and H. Schmidt-Böcking, Rep. Prog. Phys. **66**, 1463 (2003).

[32] M. Busuladžić, A. Gazibegović-Busuladžić, D. B. Milošević, and W. Becker, Phys. Rev. Lett. **100**, 203003 (2008).

[33] M. Busuladzic, A. Gazibegovic-Busuladzic, D. B. Milosevic, and W. Becker, Phys. Rev. A **78**, 033412 (2008).

[34] M. Busuladžić and D. B. Milošević, Phys. Rev. A **82**, 015401 (2010).

[35] V. I. Usachenko and S.-I. Chu, Phys. Rev. A **71**, 063410 (2005).

[36] W. Quan, X. Y. Lai, Y. J. Chen, C. L. Wang, Z. L. Hu, X. J. Liu, X. L. Hao, J. Chen, E. Hasović, M. Busuladžić, W. Becker, and D. B. Milošević, Phys. Rev. A **88**, 021401(R) (2013).

[37] M. Okunishi, R. Itaya, K. Shimada, G. Prümper, K. Ueda, M. Busuladžić, A. Gazibegović-Busuladžić, D. B. Milošević, and W. Becker, Phys. Rev. Lett. **103**, 043001 (2009).

[38] P. B. Corkum, N. H. Burnett, and F. Brunel, Phys. Rev. Lett. **62**, 1259 (1989).